



## OPEN ACCESS

## EDITED BY

Fang Bian,  
The University of Texas at Dallas, United States

## REVIEWED BY

Guilherme Baldo,  
Federal University of Rio Grande do Sul, Brazil  
Robert J. Huber,  
Trent University, Canada

## \*CORRESPONDENCE

Bogdan Budnik  
✉ bogdan.budnik@wyss.harvard.edu  
Yulia Grishchuk  
✉ ygrishchuk@amgh.harvard.edu

†These authors have contributed equally to this work and share first authorship

†These authors have contributed equally to this work and share senior authorship

RECEIVED 01 May 2023

ACCEPTED 17 July 2023

PUBLISHED 07 August 2023

## CITATION

Sangster M, Shahriar S, Niziolek Z, Carisi MC, Lewandowski M, Budnik B and Grishchuk Y (2023) Brain cell type specific proteomics approach to discover pathological mechanisms in the childhood CNS disorder mucopolidosis type IV. *Front. Mol. Neurosci.* 16:1215425. doi: 10.3389/fnmol.2023.1215425

## COPYRIGHT

© 2023 Sangster, Shahriar, Niziolek, Carisi, Lewandowski, Budnik and Grishchuk. This is an open-access article distributed under the terms of the [Creative Commons Attribution License \(CC BY\)](https://creativecommons.org/licenses/by/4.0/). The use, distribution or reproduction in other forums is permitted, provided the original author(s) and the copyright owner(s) are credited and that the original publication in this journal is cited, in accordance with accepted academic practice. No use, distribution or reproduction is permitted which does not comply with these terms.

# Brain cell type specific proteomics approach to discover pathological mechanisms in the childhood CNS disorder mucopolidosis type IV

Madison Sangster<sup>1†</sup>, Sanjid Shahriar<sup>2†</sup>, Zachary Niziolek<sup>3</sup>, Maria Carla Carisi<sup>1</sup>, Michael Lewandowski<sup>2</sup>, Bogdan Budnik<sup>2\*†</sup> and Yulia Grishchuk<sup>1\*†</sup>

<sup>1</sup>Center for Genomic Medicine and Department of Neurology, Massachusetts General Hospital Research Institute and Harvard Medical School, Boston, MA, United States, <sup>2</sup>Wyss Institute for Biologically Inspired Engineering, Harvard University, Boston, MA, United States, <sup>3</sup>Bauer Flow Cytometry Core, Harvard University, Cambridge, MA, United States

Mucopolidosis IV (MLIV) is an ultra-rare, recessively inherited lysosomal disorder resulting from inactivating mutations in *MCOLN1*, the gene encoding the lysosomal cation channel TRPML1. The disease primarily affects the central nervous system (CNS) and manifests in the first year with cognitive and motor developmental delay, followed by a gradual decline in neurological function across the second decade of life, blindness, and premature death in third or fourth decades. Brain pathology manifestations in MLIV are consistent with hypomyelinating leukodystrophy with brain iron accumulation. Presently, there are no approved or investigational therapies for MLIV, and pathogenic mechanisms remain largely unknown. The MLIV mouse model, *Mcoln1*<sup>-/-</sup> mice, recapitulates all major manifestations of the human disease. Here, to better understand the pathological mechanisms in the MLIV brain, we performed cell type specific LC-MS/MS proteomics analysis in the MLIV mouse model and reconstituted molecular signatures of the disease in either freshly isolated populations of neurons, astrocytes, oligodendrocytes, and neural stem cells, or whole tissue cortical homogenates from young adult symptomatic *Mcoln1*<sup>-/-</sup> mice. Our analysis confirmed on the molecular level major histopathological hallmarks of MLIV universally present in *Mcoln1*<sup>-/-</sup> tissue and brain cells, such as hypomyelination, lysosomal dysregulation, and impaired metabolism of lipids and polysaccharides. Importantly, pathway analysis in brain cells revealed mitochondria-related alterations in all *Mcoln1*<sup>-/-</sup> brain cells, except oligodendrocytes, that was not possible to resolve in whole tissue. We also report unique proteome signatures and dysregulated pathways for each brain cell population used in this study. These data shed new light on cell-intrinsic mechanisms of MLIV and provide new insights for biomarker discovery and validation to advance translational studies for this disease.

## KEYWORDS

lysosomal disease, mucopolidosis, TRPML1, central nervous system, brain cells, cell specific proteomics, biomarkers

## 1. Introduction

Mucopolidosis type 4 (MLIV) is a lysosomal disease that affects the central nervous system and is inherited in an autosomal-recessive manner. The typical form of MLIV, caused by the absence of functional TRPML1 protein or its complete loss of function, is characterized by hypomyelinating leukodystrophy with brain iron accumulation and manifests with severely impaired psychomotor development and a gradual neurological decline paralleled by cerebellar neurodegeneration and neuroaxonal injury (Frei et al., 1998; Bonavita et al., 2003; Schiffmann et al., 2014). Retinal dystrophy also develops in the first years of life and leads to blindness by the second decade. Brain MRI abnormalities in childhood include marked hypoplasia of the corpus callosum, decreased subcortical white matter, ferritin deposition in the basal ganglia, and relative preservation of cortical gray matter. Later in the course of disease, over the first two decades, the cerebellum degenerates, and, eventually, diffuse cerebral atrophy may become apparent (Frei et al., 1998; Schiffmann et al., 2014).

Although it is not fully understood how early brain development is affected in MLIV, subcortical hypomyelination and iron accumulation in the basal ganglia have been reported in MLIV at gestational stage (Zerem et al., 2021). Despite this early evidence of brain pathology, patients generally achieve their developmental motor milestones up to 6 months of age and present with hypotonia and delayed gross motor development around 1 year of age (Chitayat et al., 1991; Altarescu et al., 2002). Corneal opacities often present from birth, elevated plasma gastrin, and delayed neuromotor development in infants warrant genetic testing and are suggestive of MLIV. Most patients do not achieve independent ambulation. Motor development in MLIV is negatively impacted by both pyramidal and extrapyramidal tract dysfunction. The pyramidal signs, such as spasticity, gradually increase in severity across the lifetime. The extrapyramidal motor signs are typically present in the first year of life, but progressively worsening spasticity makes the presence of extrapyramidal signs difficult to discern later in life, and their progression remains unstudied. Cognitive development in patients with MLIV is difficult to assess due to motor, expressive language, and visual impairment.

Most of the known patients with MLIV exhibit the typical severe form, which is associated with variants that completely abolish TRPML1 function or prevent its production (Misko et al., 1993; Altarescu et al., 2002). Therefore, conventional knockout of *Mcoln1* presents a relevant approach to create preclinical model of this disease. Indeed, *Mcoln1* knock out mice exhibit all major symptoms of MLIV, including cognitive and motor dysfunction, brain and eye pathology, and elevated plasma gastrin (Venugopal et al., 2007; Grishchuk et al., 2014, 2015, 2016). *Mcoln1*<sup>-/-</sup> mice develop cognitive and motor deficits by 2 months of age, with subsequent progression of motor dysfunction evident through rotarod and balance beam tests. Motor deficits progress to rear limb paralysis by 7 months, and premature death occurs a few weeks later (Venugopal et al., 2007; Boudewyn et al., 2017).

Brain histopathology in *Mcoln1*<sup>-/-</sup> mice shows many characteristics seen in other mouse models of lysosomal disorders, such as an accumulation of autofluorescent material, neuronal accumulation of gangliosides and cholesterol, and increased autophagy substrate P62/SQSTRM, indicating inhibited autophagic

and lysosomal function. All human brain pathology hallmarks of MLIV such as decreased myelination, glial activation and partial Purkinje neurons loss in late-stage cerebellum are also present in *Mcoln1*<sup>-/-</sup> mice (Micsenyi et al., 2009; Boudewyn et al., 2017). Interestingly, many of the pathological hallmarks present in the *Mcoln1*<sup>-/-</sup> brain at the terminal stage, i.e., gliosis, hypomyelination, and lysosomal material accumulation, are already present as early as at post-natal day 10, prior to onset of the first detectable motor dysfunction (Boudewyn et al., 2017). Remarkably, *Mcoln1*<sup>-/-</sup> mice do not show significant brain atrophy or neuronal loss throughout the course of the disease, except for the partial loss of Purkinje cells in the cerebellum mentioned earlier (Grishchuk et al., 2014; Boudewyn et al., 2017). These findings, along with the data from MLIV patients, suggest that TRPML1 plays an essential role in early brain development, and that loss of its function leads to widespread brain pathology and dysfunction of various brain cell types but does not cause overt neurodegeneration.

Overall, histological analysis of *Mcoln1*<sup>-/-</sup> brain and studies on isolated cells indicate that all brain cell types are affected by loss of TRPML1 function (Grishchuk et al., 2014, 2015), yet resolution of these changes on the molecular level and understanding of the functional impact of TRPML1 loss in major brain cell types is missing. Here, we set out to reconstitute the proteomic profiles of whole cortical tissue and freshly isolated neurons, neural stem cells, oligodendrocytes, microglia, and astrocytes from *Mcoln1*<sup>-/-</sup> and control littermates at the early symptomatic stage of disease at 3 months. Our data confirmed on the molecular level major histopathological hallmarks of MLIV universally present in *Mcoln1*<sup>-/-</sup> tissue and brain cells, such as hypomyelination, lysosomal dysregulation, and impaired metabolism of lipids and polysaccharides. We report unique proteome signatures and dysregulated pathways for each brain cell population including neurons, neuronal precursors, oligodendrocytes, microglia and astrocytes. Proteomics analysis of these isolated brain cells revealed mitochondria-related alterations in all *Mcoln1*<sup>-/-</sup> brain cells, except oligodendrocytes, that was not possible to resolve in whole tissue. These data shed new light on cell-intrinsic mechanisms of MLIV and provide new insights for biomarker discovery and validation to advance translational studies for this disease.

## 2. Materials and methods

### 2.1. Animals

*Mcoln1*<sup>-/-</sup> mice (RRID:IMSR\_JAX:027110) were maintained as previously described (Venugopal et al., 2007). Genotyping was performed by Transnetyx using real-time qPCR.<sup>1</sup> The *Mcoln1*<sup>+/-</sup> breeders for this study were obtained by backcrossing onto a C57BL/6 J background for more than 10 generations. Experimental cohorts were obtained from *Mcoln1*<sup>+/-</sup> x *Mcoln1*<sup>-/-</sup> mating. *Mcoln1*<sup>+/-</sup> and *Mcoln1*<sup>+/+</sup> littermates were used as controls. Experiments were performed according to the Institutional and National Institutes of Health guidelines and approved by the Massachusetts General

<sup>1</sup> [www.transnetyx.com](http://www.transnetyx.com)

Hospital Institutional Animal Care and Use Committee. Female mice were used at 3 months of age.

## 2.2. Brain tissue dissociation

Brain tissue dissociation was performed according to (Ximerakis et al., 2019) with some modifications. Immediately after euthanasia using a carbon dioxide chamber, the brain was extracted, the meninges removed, and the dissected cortex was placed in ice-cold HBSS buffer (no calcium, no magnesium, 1% GlutaMAX, 5% trehalose). After a short spin-down and removal of supernatant, the Adult Brain Dissociation kit (Miltenyi #130-107-677, RRID:SCR\_020295) was used with a few modifications to obtain a single cell solution. In enzyme mix 1, the papain concentration was halved and 5% trehalose (Sigma-Aldrich, #T0167) was added; 45uM actinomycin D (Sigma-Aldrich #SBR00013) was added to both enzyme mixes. The samples were incubated under continuous rotation at 34°C. Each enzyme mix was added separately in between incubations. The cortices were dissociated manually using a serological pipet followed by a fire-polished Pasteur pipette. 10% ovomucoid protease inhibitor (Worthington Biochemical #LK003182) was added to quench the reaction. The solution was washed with a wash buffer comprised of 0.5% BSA (Miltenyi #130-091-376), 1% GlutaMAX (Gibco # 35050061) in HBSS with calcium and magnesium (Gibco # 14185052), and cell clumps were removed with a 70um cell strainer (Miltenyi #130-098-462), then washed two more times to remove myelin and debris. Erythrocytes were removed with the Miltenyi red blood cell removal solution diluted in ddH<sub>2</sub>O and a 5-min incubation at 4°C, followed by an additional wash and spin down.

## 2.3. Cell labelling and flow cytometry

The cells were resuspended in ice-cold labelling buffer (0.1% BSA, 2 mM EDTA, 1% GlutaMAX, and 5% trehalose in HBSS without calcium or magnesium) and incubated with FcR blocking reagent (Miltenyi #130-092-575) for 10 min at 4°C in the dark under continuous rotation to reduce non-specific cell labelling. The cells were then labelled with the following antibodies: anti-ASCA-2-APC (Miltenyi #130-117-535, RRID:AB\_2727978; 1:14) for astrocytes, anti-O4-488 (R&D #FAB1326G, RRID:AB\_2936942; 1:27) for oligodendrocytes, anti-CD200-PE (Biolegend #123808, RRID:AB\_2073942;1:90) for neurons, anti-CD11b-BV510 (BD #562950, RRID:AB\_2737913; 1:90) for microglia, and anti-CD15-PerCP-eFluor710 (eBioscience #46-8,813-42, RRID:AB\_11217476; 1:22.5) for neuronal stem cells for 15 min at 4°C in the dark under continuous rotation. The cells were washed, pelleted, and resuspended in 15 ml ice-cold FACS buffer (0.5% BSA, 1% GlutaMAX, and 5% trehalose in HBSS with calcium and magnesium) per cortex. Cells were incubated with 10 µM Dycycle Violet (Thermo V35003) in the FACS tubes 15 min prior sorting to sort out cellular debris and dead cells. Live nucleated Dycycle Violet + cells were then sorted with a Moflo Astrios instrument (Beckman Coulter, RRID:SCR\_018893) with a 100 µm nozzle at 24 psi. Gates were set manually with compensation beads (Life Technologies, A10497) and appropriate control samples, and data were analyzed with FlowJo software (v.10).

## 2.4. Individual brain cell specific sample preparation

FACS sorted astrocytes, oligodendrocytes, neurons, microglia, and NSC were stored in -80°C in separate 2 ml Eppendorf tubes. For LC-MS/MS cell samples were prepared according to mPOP protocol (Specht et al., 2018). Frozen samples were placed on Corning LSE Digital Dry Bath at 95°C for 5 min. Samples were immediately placed on ice bath for 5 min. **Digestion:** A stock solution of Trypsin Platinum, Mass Spec Grade (Promega) was made up at 100µg/ml in 50 mM TEAB. A specific volume of stock trypsin was added to each sample vial for each set of brain cells using a 1:50 ratio (Trypsin:Protein). Samples were incubated for 2 h at 50°C and shaken/mixed at 350 rpm on Eppendorf ThermoMixer C. **TMT Labeling:** Samples, now peptides, were labeled using 4 µl of TMTpro Mass Tag Labels (ThermoScientific). After labeling, samples were then placed on Eppendorf ThermoMixer C for 45 min and shaken/mixed for 45 min; this ensures labels are covalently bonded to peptides. Labeling reaction was quenched for 10 min using 1 µl of 5% hydroxyamine. After quenching, all individually labeled samples were pooled into one 2 ml Eppendorf tube and then dried down using Eppendorf Vacufuge plus. **Desalting Samples:** Dried samples were resuspended in 300 µl of 0.1% TFA in ultrapure HPLC grade water and vortexed to ensure full solubility. Samples were then desalted using Pierce™ Peptide Desalting Spin Columns (ThermoScientific). Final eluate (desalted samples) contained 600 µl of 50% HPLC grade Acetonitrile & 50% ultrapure HPLC grade water. Desalted samples were then transferred to HPLC vials and were dried down using Eppendorf Vacufuge plus. Dried and desalted samples were resuspended in 6 µl of 0.1% Formic Acid in ultrapure HPLC grade water and were then injected on LC-MS/MS.

## 2.5. Brain tissue preparation

Brain tissue was stored in -80°C in 2 ml Eppendorf tubes. **Protein Extraction Protocol:** Samples were placed on dry ice and frozen brain tissue was ground up inside the tube using pestle. 130 µl of 5% SDS was then added to ground up tissue. Samples were centrifuged at 15,000 g for 5 min on Eppendorf Centrifuge 5,420 (further in methods referred as “centrifuge”). Supernatant (100 µl) was then transferred to new 2 ml Eppendorf tubes. The remaining 30 µl was stored in -80°C for future work. **Reduction/Alkylation and Acidification:** 8.7 µl of 10 mM TCEP was added to each sample, samples were shaken/mixed for 30 min at 350 rpm on Eppendorf ThermoMixer C (further referred as “mixer”). 8.7 µl of 10 mM IAA was added to reduced samples followed by 10 min of shaking at 350 rpm mixer, after that 21.7 µl of 12.5% Phosphoric Acid was added. **Trap and Clean Protein Protocol:** 1522 µl of Binding/Wash Buffer (100 mM TEAB in 90% Methanol) was added with immediate vortexing; sample visually appeared as milky colloidal suspension. Colloidal suspension was trapped by transferred to S-Trap mini column and centrifuged at 4,000 g for 30s on centrifuge; flow through discarded. Protein was cleaned on S-Trap mini column (Protifi, MA) by washing with 1522 µl Binding/Wash Buffer and centrifuged at 4,000 g for 30s; this was repeated for total of 3X and each flow through was discarded. 3X cleaning in previous step is critical as it ensures SDS is washed from protein sample.

**Digestion:** A stock solution of Trypsin Platinum, Mass Spec Grade (Promega, WA) was made up at 100ug/ml in 50 mM TEAB. A specific volume of stock trypsin was added directly to the top of each S-Trap mini column using a 1:50 ratio (Trypsin:Protein). Samples were incubated for 2 h at 50°C and shaken/mixed at 350 rpm on mixer. **Elute Peptides:** Elution 1: After digestion was completed, 80 µl of 50 mM TEAB in water (pH 8.5) was added directly to each S-Trap mini column and then centrifuged at 4,000 g for 1 min; flow through containing peptides was set aside. Elution 2: 80 µl of 0.2% Formic Acid added directly to each S-Trap mini column and then centrifuged at 4,000 g for 1 min on centrifuge; flow through containing peptides was set aside. Elution 3: 80 µl of 50% Acetonitrile in water was added directly to each S-Trap mini column and then centrifuged at 4,000 g for 1 min; flow through containing peptides was set aside. For each sample, the 3 elutions were combined and set aside for TMT labeling. **TMT Labeling:** Samples, now peptides, were labeled using 40 µl of TMTpro Mass Tag Labels (ThermoScientific, CA). After labeling, samples were placed on mixer for 45 min; this ensures labels are covalently bonded to peptides. Labeling reaction was quenched for 10 min using 8 µl of 5% hydroxylamine. After quenching, samples were pooled into one 2 ml Eppendorf tube and then dried down using Eppendorf Vacufuge plus. **Fractionation:** Dried samples were resuspended in 120 µl of 0.1% TFA in ultrapure HPLC grade water and vortexed to ensure full solubility. Samples were then fractionated using Pierce™ High pH Reversed-Phase Peptide Fractionation Kit Columns (ThermoScientific). Each fraction contained 120 µl of volume for a total of 20 fractions. Each fraction was centrifuged at 3,000 g for 2 min; flow throughs collected and transferred to HPLC vials. All fractions were dried down using Eppendorf Vacufuge plus and resuspended in 6 µl of 0.1% Formic Acid in water (ThermoScientific, CA) and were then injected on LC-MS/MS.

## 2.6. Mass spectrometry analysis

After separation each fraction was submitted for single LC-MS/MS experiment that was performed on an Exploris 240 Orbitrap (Thermo Scientific, RRID:SCR\_022216) equipped with NEO (Thermo Scientific) nanoHPLC pump. Peptides were separated onto a 300 µm x 5 mm PepMap C18 trapping column (Thermo Scientific, Lithuania) followed by DNV PepMap Neo 75µmx150mm analytical column (Thermo Scientific, Lithuania). Separation was achieved through applying a gradient from 5–25% ACN in 0.1% formic acid over 120 min at 250 nl/min. Electrospray ionization was enabled through applying a voltage of 1.8 kV using a PepSep electrode junction at the end of the analytical column and sprayed from stainless steel PepSep emitter SS 30 µm LJ (Odense, Denmark). The Exploris Orbitrap was operated in data-dependent mode for the mass spectrometry methods. The mass spectrometry survey scan was performed in the Orbitrap in the range of 450–900 m/z at a resolution of  $1.2 \times 10^5$ , followed by the selection of the 10 most intense ions (TOP10) ions were subjected to HCD MS2 event in Orbitrap part of the instrument. The fragment ion isolation width was set to 0.8 m/z, AGC was set to 50,000, the maximum ion time was 150 ms, normalized collision energy was set to 34 V and an activation time of 1 ms for each HCD MS2 scan.

## 2.7. Mass spectrometry data analysis

Raw data were submitted for analysis in Proteome Discoverer 3.0.1.23 (Thermo Scientific, RRID:SCR\_014477) software with Chimerys. Assignment of MS/MS spectra was performed using the Sequest HT algorithm and Chimerys (MSAID, Germany) by searching the data against a protein sequence database including all entries from the Mouse Uniprot database (SwissProt 197,682,019; RRID:SCR\_002380) and other known contaminants such as human keratins and common lab contaminants (for details see [Supplementary file](#) “Contaminants”). Sequest HT searches were performed using a 20 ppm precursor ion tolerance and requiring each peptides N-/C termini to adhere with Trypsin protease specificity, while allowing up to two missed cleavages. 18-plex TMT tags on peptide N termini and lysine residues (+304.207146 Da) was set as static modifications and Carbamidomethyl on cysteine amino acids (+57.021464 Da) while methionine oxidation (+15.99492 Da) was set as variable modification. A MS2 spectra assignment false discovery rate (FDR) of 1% on protein level was achieved by applying the target-decoy database search. Filtering was performed using a Percolator [64bit version, reference ([Bonavita et al., 2003](#))]. For quantification, a 0.02 m/z window centered on the theoretical m/z value of each of the six reporter ions and the intensity of the signal closest to the theoretical m/z value was recorded. Reporter ion intensities were exported in result file of Proteome Discoverer 3.0 search engine as an excel tables. The total signal intensity across all peptides quantified was summed for each TMT channel, and all intensity values were adjusted to account for potentially uneven TMT labeling and/or sample handling variance for each labeled channel. Proteins with single peptide were accepted as positively identified proteins.

Proteomics spectral matching (PSM) level data obtained from each TMT channel was subjected to comprehensive analysis in R. The datasets were preprocessed by first imputing missing values with random forest, followed by removal of PSMs that had no data on isolation interference, or showed isolation interference values greater than 70, or were mapped to multiple proteins or no proteins at all. The preprocessed PSM level data was then aggregated to the protein level and normalized using the variance stabilizing normalization method. Differential expression analysis was performed using the R limma package to compare the *Mcoln1*<sup>-/-</sup> mouse brain tissue/cell types against their control counterparts. To visualize the results, volcano plots were generated for each dataset, emphasizing proteins that were up- or downregulated 1.5-fold in the mutants relative to the wild-type samples, and were significantly different at *p* values <0.1. The *p*-value threshold was set at 0.1 with the specific intention to increase the sensitivity of our analyses and enhance our ability to identify differentially expressed proteins. Given the exploratory nature of our study, we considered this approach to be a reasonable balance between sensitivity and specificity, particularly in the context of the small number of significant proteins we identified at the 0.05 level. The overlap in significantly up- and downregulated proteomic signatures among the five brain cell types and brain tissue were visualized using Venn Diagrams.<sup>2</sup> Lastly, the Database for Annotation, Visualization and Integrated Discovery (DAVID; RRID:SCR\_001881)

<sup>2</sup> <https://bioinformatics.psb.ugent.be/webtools/Venn/>

Bioinformatics functional annotation tool was used to identify signaling pathways, metabolic pathways and protein interactions enriched in *Mcoln1*<sup>-/-</sup> brain tissue and cell types relative to their control counterparts. Pathways with FDR ≤ 0.05 were deemed to be significantly altered.

## 2.8. MCOLN1 gene transfer experiment in *Mcoln1*<sup>-/-</sup> mice

scAAV9-JeT-MCOLN1 vector was prepared and used for intracerebroventricular injections in neonatal *Mcoln1*<sup>-/-</sup> and *Mcoln1*<sup>+/-</sup> control littermates at post-natal day 1 at a dose of 3e10vg/mouse using our standard previously described procedures (De Rosa et al., 2021). At the age of 3 months mice were sacrificed and brain tissues were collected for post-mortem evaluation using Western blotting.

## 2.9. Western blot analysis

For immunoblotting fresh-frozen pieces of sensory-motor cortex were homogenized in the lysis buffer (20 mmol/L HEPES, pH 7.4, 10 mmol/L NaCl, 3 mmol/L MgCl<sub>2</sub>, 2.5 mmol/L EGTA, 0.1 mmol/L dithiothreitol, 50 mmol/L NaF, 1 mmol/L Na<sub>3</sub>VO<sub>4</sub>, 1% Triton X-100 (reagents from Sigma, LaJolla, CA, USA), and a protease inhibitor cocktail (Roche, 11,873,580,001, Mannheim, Germany)). Homogenates were centrifuged at 5,000 rpm for 10 min at 4°C, supernatants collected, and protein concentration was determined using Pierce BSA Protein Assay kit (ThermoFisher Scientific, Waltham, MA, USA). Proteins (20 µg/sample) were separated by SDS-PAGE on a 4–12% Bis-Tris gels 3-(N-morpholino)propansulfonic acid (MOPS) buffer (Bio-Rad Laboratories, USA) and transferred onto nitrocellulose membrane (ThermoFisher Scientific, Waltham, MA, USA). The following primary antibodies were used: anti-tryptidyl peptidase 1 (ab96498, 1/2000, rabbit polyclonal, Abcam, Cambridge, MA, USA), anti-β-actin (A5441, 1/5000, mouse monoclonal, Sigma, LaJolla, CA, USA). After incubation with primary antibody, the secondary polyclonal goat anti-mouse or goat anti-rabbit IgG antibodies conjugated with IRDye 680 or IRDye 800 from LI-COR (Lincoln, NE, USA) were applied. Protein bands were visualized using the Odyssey Infrared Imaging System (LI-COR, Lincoln, NE, USA). In densitometric analysis OD values were normalized by β-actin. All data were expressed as mean ± SEM; n (*Mcoln1*<sup>+/-</sup> saline) = 5; n (*Mcoln1*<sup>-/-</sup> saline) = 6; n (*Mcoln1*<sup>-/-</sup> AAV9-MCOLN1) = 5. Data were analyzed statistically by the ordinary one-way ANOVA test with correction for multiple comparisons using Dunnett test in GraphPad Prism software v.9 (San Diego, CA, USA).

## 3. Results

To resolve cell type specific proteomes in adult mouse brain in symptomatic *Mcoln1*<sup>-/-</sup> (*n* = 5) and control mice (*n* = 5), pieces of cortical tissue were individually homogenized and cells were freshly isolated using an optimized protocol detailed in Material and Methods, labeled with cell type specific fluorophore-conjugated antibodies (anti-ASCA-2 for astrocytes, anti-O4 for oligodendrocytes, anti-CD200 for neurons, anti-CD11b for microglia, and anti-CD15

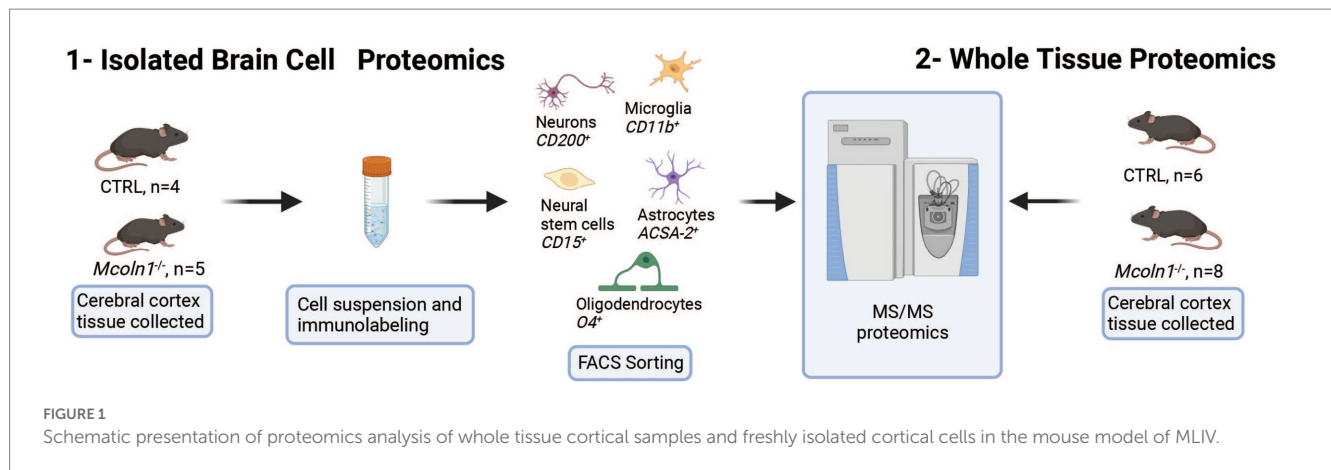
for neuronal stem cells), collected using fluorescence activated cell sorting (FACS), and frozen (Figure 1). Since brain cells in the adult brain are highly interconnected and have extensive branches and complex morphology, fresh isolation of cells presents a challenge and often leads to breakage and loss of the distant cellular parts. Despite these challenges with isolating brain cells from the adult brain tissue, cell counts for all cell types after FACS sorting (Supplementary Table 1) were sufficient for LC-MS/MS proteomics analysis. In one of the control brain samples, low cell counts were obtained for all five types of brain cells, and this mouse was removed from the follow-up data analysis.

To investigate proteomes in the whole brain tissue, identical parts of cerebral cortex were extracted from the age- and sex-matched *Mcoln1*<sup>-/-</sup> and control mice and snap-frozen on dry ice. Frozen brain tissue was mechanically homogenized, centrifuged, and clarified tissue homogenates were digested and eluted peptides were labeled by TMTpro and subsequently separated to 20 fractions. All fractions were dried and, after solubilization in Formic acid, run on mass spectrometer for LC-MS/MS analysis.

## 3.1. Whole tissue and cell type specific proteomes

LC-MS/MS proteomics analysis identified 7,397 proteins from Uniprot mouse and in-house made contaminants databases in the whole tissue cortical homogenates, 446 in neurons, 217 in neural stem cells, 378 in oligodendrocytes, 1985 in astrocytes and 387 in microglia (Supplementary Table 2). All detected non-mouse protein contaminants, as well as mouse albumin and keratin entries were removed from these data sets (the list of all typical contaminants is available in Supplementary Table 3). Principal component analysis (PCA) separated *Mcoln1*<sup>-/-</sup> samples from controls in all sample sets (Supplementary Figure 1). Comparison analysis of whole tissue data set revealed 29 downregulated and 26 upregulated proteins in *Mcoln1*<sup>-/-</sup> cortical tissue as compared to control littermates with log<sub>2</sub> foldchange cutoff at 0.6 (foldchange of +/-1.5) and adjusted log<sub>10</sub> *p* < 1 (*p*-value <0.1; Figures 2A,B). Among these downregulated proteins, 17 were either myelin or oligodendrocyte lineage enriched proteins (blue asterisks, Figure 2B). Remarkably, the whole tissue upregulated proteome in *Mcoln1*<sup>-/-</sup> mice was dominated by lysosomal proteins (16 out of 26; red asterisks, Figure 2B).

To reveal how loss of TRPML1 affects different brain cell types, we performed comparative analysis of protein abundancies between control and *Mcoln1*<sup>-/-</sup> samples for each cell type (Figure 3; Supplementary Table 2). The highest number of differentially expressed proteins was detected in astrocytes (74 upregulated; 82 downregulated) and microglia (45 upregulated; 47 downregulated), whereas neurons, neuronal stem cells, and oligodendrocytes showed lower number of differential proteins (13, 27, and 13 upregulated; 17, 26, and 5 downregulated per cell type, respectively). We have noticed the presence of histones among the top five upregulated proteins in neural stem cells and glia, i.e., oligodendrocytes, microglia, and astrocytes, suggestive of active chromatin reorganization, DNA replication, and potentially increased division of the corresponding cell types (Figure 3). Interestingly, despite broad downregulated myelin signature in the whole brain tissue, only a few differentially expressed proteins were detected in the isolated *Mcoln1*<sup>-/-</sup> vs. control



oligodendrocytes. Among 17 detected myelin and oligodendrocytes enriched proteins downregulated in the MLIV whole tissue samples, 7 (PLP, MOG, Alpha-Crystallin, MOBP, JAMC, Ermin and CNPase) were resolved in isolated oligodendrocytes but showed no significant changes (Supplementary Table 2). This may indicate that reduced levels of these proteins in whole tissue samples indicate reduced numbers of differentiated oligodendrocytes in the MLIV brain, while isolated O4<sup>+</sup> *Mcoln1*<sup>-/-</sup> oligodendrocytes did not exhibit major cell-intrinsic proteome changes in response to TRPML1 loss.

Comparative analysis of overlapping up- and downregulated proteins between reconstituted whole tissue vs. isolated brain cells proteomes showed no common downregulated and only two common upregulated proteins (Figures 4A,B).

Remarkably, the two commonly upregulated proteins are lysosomal enzymes, tripeptidyl-peptidase 1 (TPP1) and beta-hexosaminidase (HEXB). Upregulation of these lysosomal enzymes across all brain samples confirms that lysosomal dysregulation is a universal cell pathologic mechanism of MLIV. The upregulation of TPP1 and HEXB in MLIV across all sample types suggests that these proteins could be promising candidates for further investigation as potential biomarkers. They could serve to monitor lysosomal dysregulation and, potentially, assess its restoration in the MLIV mouse model. To validate these findings, we conducted Western blot analysis of TPP1 in cortical tissue homogenates (Figure 5). TPP1 is a lysosomal protease synthesized as an inactive zymogen (~60 kDa) that requires an autocatalytic cleavage of its N-terminal fragment in acidic pH of the lysosome for conversion to active serine protease (~40 kDa; Lin et al., 2001). Consistent with the increased TPP1 levels detected by LC-MS-MS, we observed a significant increase in the active form of TPP1 in *Mcoln1*<sup>-/-</sup> cortical tissue through Western blotting. Additionally, AAV-mediated gene transfer of human *MCOLN1* into *Mcoln1*<sup>-/-</sup> mice previously shown by our group to prevent motor dysfunction and restore brain pathology in *Mcoln1*<sup>-/-</sup> mice (De Rosa et al., 2021) restored levels of TPP1 in the cortical tissue. This data provide strong rationale for further investigating TPP1 as a molecular surrogate biomarker of lysosomal dysregulation in MLIV.

Overall, we found very few individual proteins overlapping among isolated neurons, neuronal stem cells, oligodendrocytes, microglia, and astrocytes in either upregulated or downregulated data sets (Figures 4C,D), with the highest number of common up- and downregulated proteins of only 3 and 4, correspondingly, found between microglia and astrocytes. Information on nonoverlapping

up- and downregulated proteins for each cell type is available in Supplementary Table 4.

## 3.2. Pathway enrichment analysis

### 3.2.1. Pathway enrichment analysis in whole tissue cortical homogenates

To reconstitute affected biological processes and pathways affected in *Mcoln1*<sup>-/-</sup> brain, we performed gene set enrichment analysis using the Database for Annotation, Visualization and Integrated Discovery (DAVID) on-line portal (<https://david.ncifcrf.gov/home.jsp>; Sherman et al., 2022). In line with observations in the comparative analysis of the individual dysregulated proteins, the most significantly enriched downregulated pathways in the *Mcoln1*<sup>-/-</sup> cortex in the whole tissue samples were the ones related to white matter development, including Myelination, Oligodendrocyte differentiation, and Gliogenesis (Table 1). The whole list of pathways is available in Supplementary Table 5. Tetraspanin CD82 (UniProt P40237) is known to regulate oligodendrocyte migration and differentiation (Mela and Goldman, 2009; Mela and Goldman, 2013), and the finding of the InterPro entry IPR018503 Tetraspanin among significantly downregulated terms is in line with the general reduction of oligodendrocyte and myelination-related pathways and provides additional insight in mechanisms of the aberrant white matter development in MLIV.

Upregulated pathways in the whole tissue samples included calcium, lysosome/hydrolase, and various metabolic and catabolic pathways (Table 1; Supplementary Table 5). These findings support general knowledge about TRPML1 function as lysosomal calcium channel, confirming on the molecular level that loss of TRPML1 function leads to dysregulated Ca<sup>2+</sup> signaling and aberrant lysosomal function in MLIV. Enlargement of the lysosomal compartment caused by impaired metabolism and the accumulation of polysaccharides and lipids in lysosomes is a core characteristic of MLIV disease that is reflected in its name, and our data accurately reflect these pathological hallmarks in whole tissue proteome via upregulation of the corresponding cell pathways.

Comparative analysis of the enriched pathways in whole brain vs. brain cells showed that Myelin sheath is the only universal downregulated pathway (Figure 6A; Supplementary Table 6). Seven commonly upregulated pathways included high level structural and

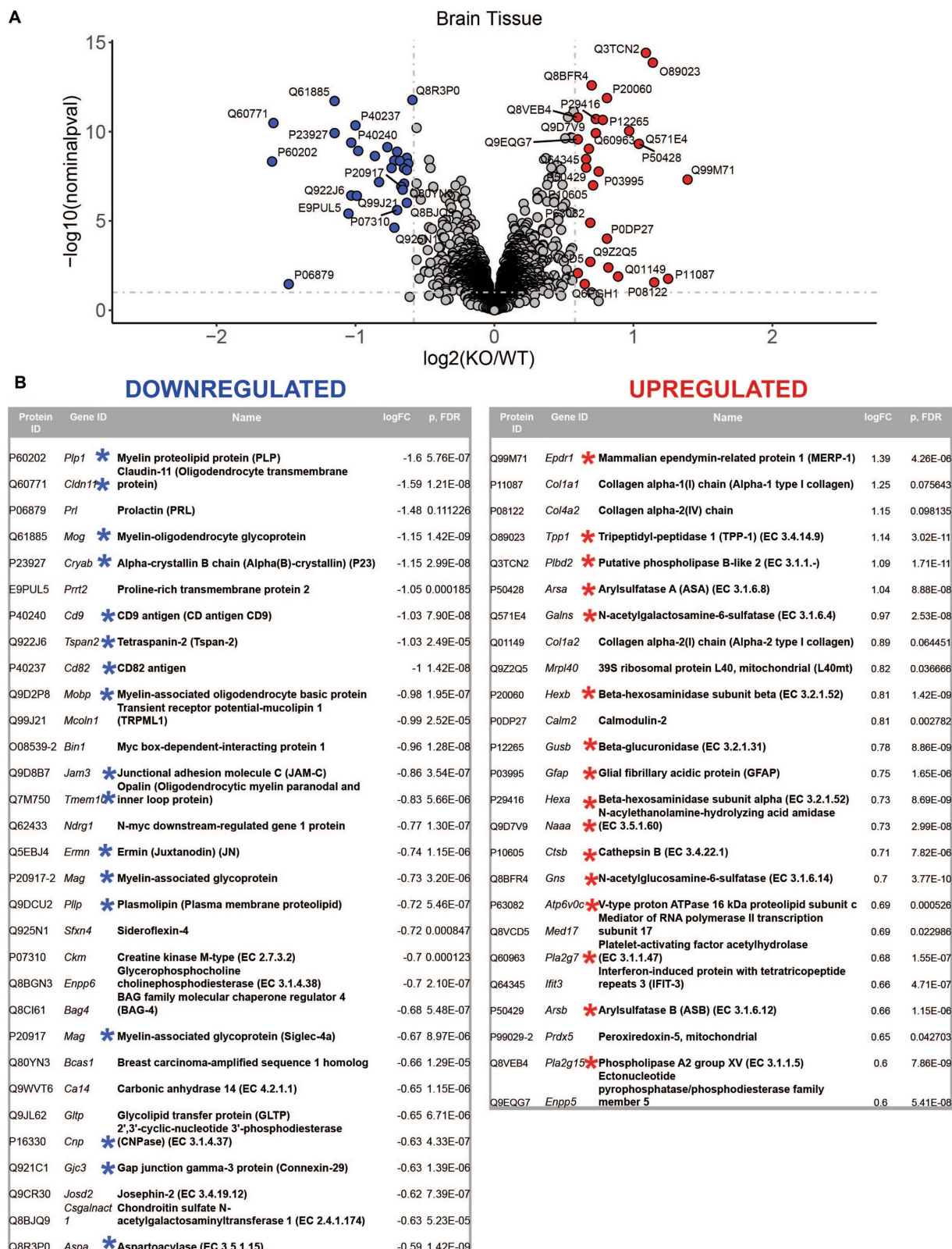


FIGURE 2

LC-MS/MS proteomics identified upregulated and downregulated proteins in whole tissue cerebral cortex homogenates from *Mcoln1*<sup>-/-</sup> mice.

(A) Volcano plot showing upregulated and downregulated proteins in whole tissue homogenates from *Mcoln1*<sup>-/-</sup> and control mice;  $\log_{10} p < 0.1$ ,  $\log_2 \text{FC} > 0.6$ . (B) List of UP and DOWN regulated proteins in whole tissue of cerebral cortex.

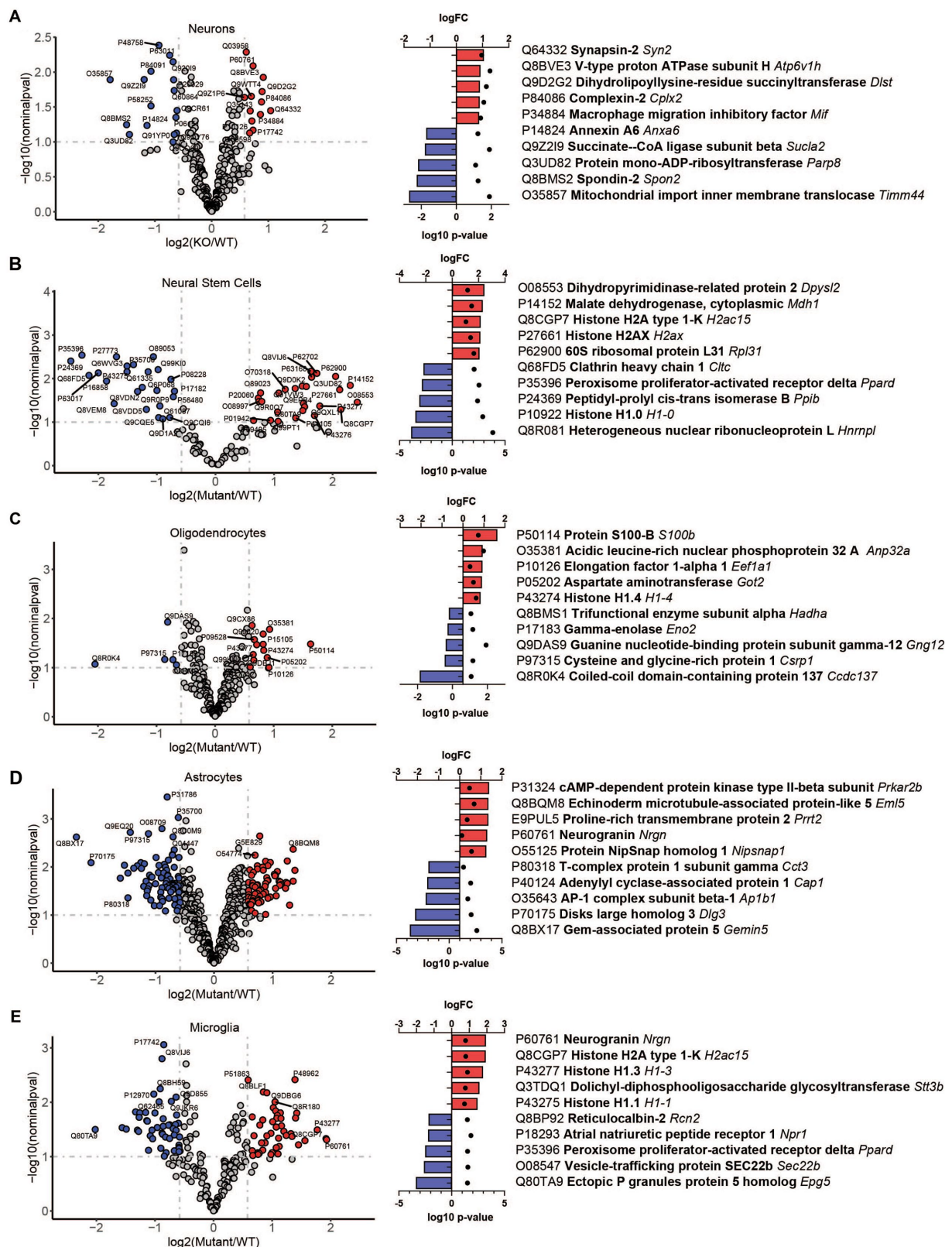
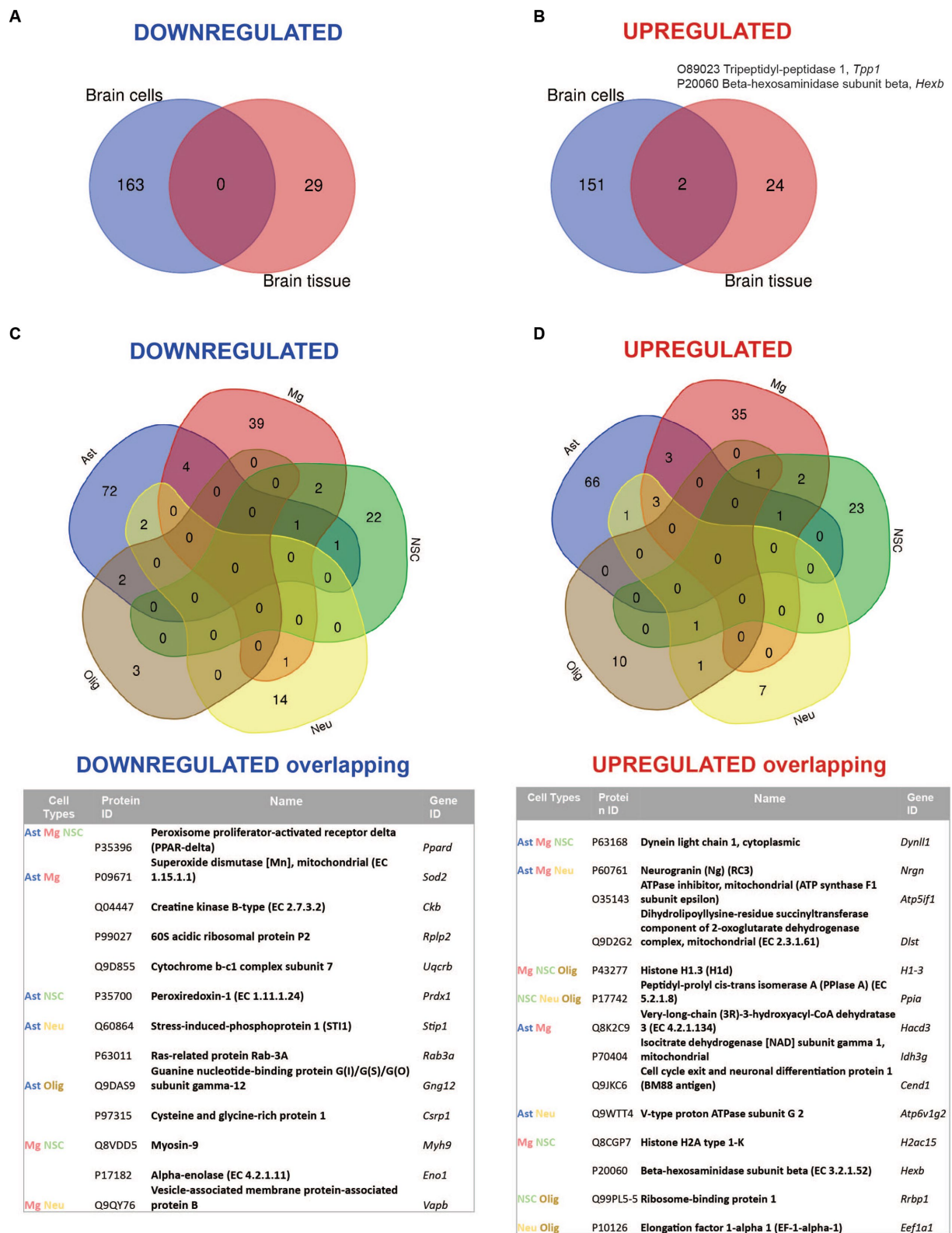


FIGURE 3

LC-MS/MS proteomics identified upregulated and downregulated proteins in isolated brain cells from *Mcoln1*<sup>-/-</sup> mice. Volcano plot of protein changes in CD200<sup>+</sup> neurons (A), CD15<sup>+</sup> neural stem cells (B), O4<sup>+</sup> oligodendrocytes (C), ACSA2<sup>+</sup> astrocytes (D) and CD11b<sup>+</sup> microglia (E) from *Mcoln1*<sup>-/-</sup> cerebral cortex; log<sub>10</sub> p < 0.1, log<sub>2</sub>FC > 0.6. Left panel show corresponding top 5 upregulated and top 5 downregulated proteins in each data set.





**FIGURE 4** Summary of comparative proteomic analysis showing common and unique findings in whole tissue and isolated brain cells from *Mcoln1*<sup>-/-</sup> mice. (A) Venn diagram of common downregulated proteins found in all separate brain cells vs. cortical brain tissue homogenates in *Mcoln1*<sup>-/-</sup> mice. (B) Venn diagram of common upregulated proteins found in all separate brain cells vs. cortical brain tissue homogenates in *Mcoln1*<sup>-/-</sup> mice. (C) Venn diagram and list of common downregulated proteins found in all separate brain cells isolated from *Mcoln1*<sup>-/-</sup> cerebral cortex. (D) Venn diagram and list of common upregulated proteins found in all separate brain cells isolated from *Mcoln1*<sup>-/-</sup> cerebral cortex.

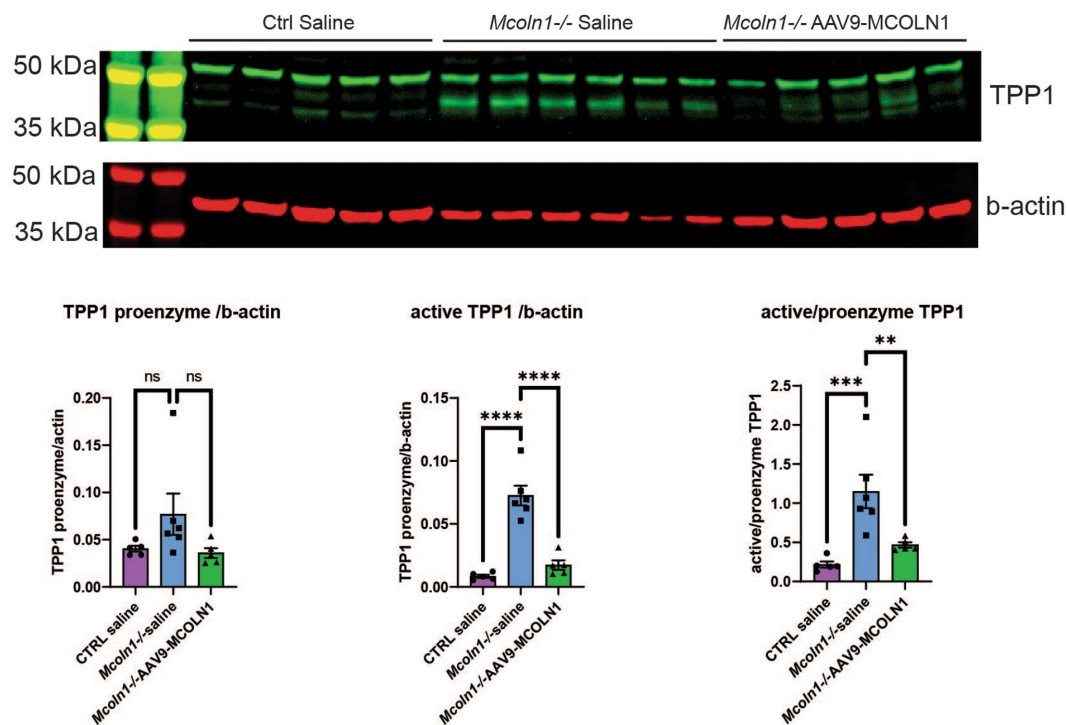


FIGURE 5

Western blot analysis in the cortical homogenates shows an increase of the active TPP1 in *Mcoln1*<sup>-/-</sup> mouse brain tissue. Immunoblot analysis of mouse cortical homogenates reveals the bands consistent with the pro-enzyme and active self-cleaved forms of TPP1. Beta-actin was used as the loading control for normalization. Quantification analysis shows significant increase of the shorter TPP1 band normalized by beta-actin and short to full-length TPP1 ratio in saline-treated *Mcoln1*<sup>-/-</sup> mice and their correction in the *Mcoln1*<sup>-/-</sup> with AAV-mediated gene transfer of human *MCOLN1*. All data expressed as mean  $\pm$  SEM; *n* (*Mcoln1*<sup>-/-</sup> saline) = 5; *n* (*Mcoln1*<sup>-/-</sup> saline) = 6; *n* (*Mcoln1*<sup>-/-</sup> AAV9-MCOLN1) = 5. Data analyzed by the ordinary one-way ANOVA test with correction for multiple comparisons by Dunnett test.

metabolic terms such as Cytoplasmic part, Intracellular membrane-bound organelle, Secretory vesicle, Cellular metabolic process, and Lipid metabolism (Figure 6B; Supplementary Table 6).

### 3.2.2. Commonly enriched pathways in isolated brain cells

We found no downregulated enriched pathways in isolated oligodendrocytes. Interestingly, Mitochondrion was the only significantly downregulated common term among the four other types of isolated brain cells (Figure 6C), and the only downregulated pathway enriched in neurons. The broadest overlap in common downregulated pathways was detected between *Mcoln1*<sup>-/-</sup> astrocytes and microglia. Both cell types demonstrated enrichment of pathways associated with major neurodegenerative diseases such as Parkinson, Alzheimer, Huntington, Prion Diseases, and Amyotrophic Lateral Sclerosis (ALS). This indicates common disease-induced signatures in astrocytic and microglial proteomes in MLIV as well as neurodegenerative settings in general.

Only one pathway was universally upregulated in all five isolated cell types from *Mcoln1*<sup>-/-</sup> mice, which is Myelin sheath. Isolated oligodendrocytes and neurons each had only one additional significantly enriched upregulated pathway; in oligodendrocytes, this was Biosynthesis of amino acids, and in neurons it was Extrinsic component of synaptic vesicle (Figure 6D and Table 2). Among other interesting findings, we found that Acetylation was upregulated in

four isolated cell types, oligodendrocytes being the exclusion. Citrullination was commonly upregulated in microglia and neural stem cells. Other preselected representative overlapping pathways are presented in Figure 6D, and the full list is available in Supplementary Table 6.

### 3.2.3. Cell-type specific enriched pathways

On top of common dysregulated pathways in *Mcoln1*<sup>-/-</sup> brain cells, our comparative analysis also revealed unique up- and downregulated pathways in different cell types (Table 2). In astrocytes, Cytoskeleton was dysregulated in both directions, likely indicating reorganization of the astrocyte cytoskeleton while it adopts proinflammatory stimulated, so-called “activated” morphology. In line with this, Cell cortex GO term, describing actin filament and its related protein network organization beneath the plasma membrane in the peripheral cytoplasm, was one of the enriched downregulated pathways, whereas actin-related Arp2/3 Protein Complex that facilitates nucleation of branched actin filaments is among enriched upregulated. Other downregulated pathways in astrocytes were related to cell homeostasis, redox stress, and detoxication which, together, manifests the stress and/or “activated” state in *Mcoln1*<sup>-/-</sup> astrocytes. Another cluster of dysregulated pathways in *Mcoln1*<sup>-/-</sup> astrocytes is related to synaptic changes, including Dendrite, Somatodendritic compartment, Post-synaptic as enriched upregulated, and Retrograde endocannabinoid signaling as enriched downregulated pathways.

**TABLE 1** Summary of representative up- and downregulated pathways in whole cortical brain homogenates from *Mcoln1*<sup>-/-</sup> mice.

Representative downregulated pathways	FDR	Representative upregulated pathways	FDR
GO:0042552 Myelination	2.35E-12	GO:0005764 Lysosome	3.37E-14
GO:0048709 Oligodendrocyte differentiation	3.15E-06	KW-0378 Hydrolase	5.39E-08
GO:0042063 Gliogenesis	4.29E-06	GO:0006027 Glycosaminoglycan catabolic process	3.79E-07
IPR018503: Tetraspanin, conserved site	0.009706	GO:0044273 Sulfur compound catabolic process	5.52E-07
		GO:0009056 Catabolic process	6.37E-06
		GO:1903510 Mucopolysaccharide metabolic process	1.22E-05
		GO:0008484 Sulfuric ester hydrolase activity	8.20E-05
		KW-0325 Glycoprotein	1.66E-04
		KW-0106 Calcium	2.16E-04
		GO:0030209 Dermatan sulfate catabolic process	9.48E-04
		GO:0016042 Lipid catabolic process	0.00355
		GO:0006665 Sphingolipid metabolic process	0.027507

In microglia, Protein synthesis, Ribosome organization, and Endoplasmic reticulum-related pathways were broadly represented and dysregulated in both directions. Additionally, a cluster of changes in post-translational protein modifications such as Isopeptide bonds, Ubl-conjugation, Nitration, and Methylation was present in downregulated pathways, whereas Hydroxylation was upregulated. Together these findings point towards dysregulated protein synthesis, homeostasis and, likely, degradation in microglia in response to TRPML1 loss. Other unique downregulated pathways in microglia included Ca<sup>2+</sup>-binding EF-hand proteins and Regulation of apoptosis. Lipid metabolism and, more specifically, fatty acid metabolism linked pathways, were broadly present in the unique upregulated group.

Unique enriched pathways in neural stem cells included Melanosome or Pigment granules, ADP binding, and Late endosome lumen. Ribosome, Protein synthesis, and Post-translational modification pathways were also significantly upregulated; in microglia, these same pathways were downregulated.

Overall, our data provide comprehensive and detailed characterization of the proteome changes in the whole brain tissue and isolated populations of brain cells that reflects previous knowledge of disease pathogenesis and provides new insights into whole brain vs. brain cell proteomes disease mechanisms, by identifying common and

revealing unique cell type specific changes in response to loss of the lysosomal channel TRPML1.

## 4. Discussion

Proteomics analysis of the brain has proved to be a powerful tool for enhancing our understanding of its functioning. Transcriptomics approaches have been widely applied across species, stages of development, and diseases to create well-resolved transcriptional brain maps as well as disease-associated transcriptional signatures (Mann et al., 2013; Wilhelm et al., 2014). However, because transcriptional and proteomic abundances show weak correlation, it is difficult to gain functional insights into brain using only transcriptome data repositories (Sharma et al., 2015). In recent years, technical advancements in proteomics have helped reconstruct and understand protein composition, expression levels, protein-protein interactions, and post-translational modifications across brain regions and cell types (Davis et al., 2018; Cookson, 2019; Drulis-Fajdasz et al., 2021; Rayaprolu et al., 2022). The purpose of this study was to determine the proteome of the brain in the mouse model of mucopolipidosis type IV, at the level of whole tissue as well as in freshly isolated neurons, astrocytes, oligodendrocytes, microglia, and neural stem cells. Data from our study confirmed known pathophysiological mechanisms of MLIV and revealed previously unknown molecular fingerprints of this disease. Remarkably, a cell-type specific proteomics approach resolved common and cell-type specific proteome changes in the *Mcoln1*<sup>-/-</sup> mouse cortex providing deeper insights on disease mechanisms, possible molecular targets, and molecular biomarker candidates for future research and validation.

### 4.1. Myelin and oligodendrocyte related changes in the *Mcoln1*<sup>-/-</sup> brain proteome

One of the most drastic features of brain pathology in MLIV is reduced myelination and dysmorphic white matter structures, particularly the corpus callosum. This places the disease in the category of hypomyelinating leukodystrophies (Misko et al., 2021; Wolf et al., 2021). Like MLIV patients, *Mcoln1*<sup>-/-</sup> mice have a dysgenic corpus callosum (Grishchuk et al., 2014, 2015). Our previous studies showed decreased expression of the mature oligodendrocyte markers myelin-associated glycoprotein precursor (*Mag*), myelin basic protein (*Mbp*), myelin-associated oligodendrocyte basic protein (*Mobp*), and myelin proteolipid protein (*Plp*) in the *Mcoln1*<sup>-/-</sup> cortex during post-natal brain development (Mepyans et al., 2020). These myelination markers were stably decreased in *Mcoln1*<sup>-/-</sup> mice in the course of disease (Grishchuk et al., 2015). Histopathological analysis in the brain showed that significant thinning of the corpus callosum in MLIV mouse is due to reduced myelination of neuronal fibers and not due to their loss (Grishchuk et al., 2015; Mepyans et al., 2020), and electron microscopy further confirmed hypomyelination via reduced myelin sheath thickness (Grishchuk et al., 2014). Reduced expression of the myelination genes *Mag*, *Mal*, *Mobp*, *Mog* and *Cnp* has recently been shown in the cerebral cortex of pre-symptomatic and symptomatic *Mcoln1*<sup>-/-</sup> mice using RNAseq (Vardi et al., 2021).

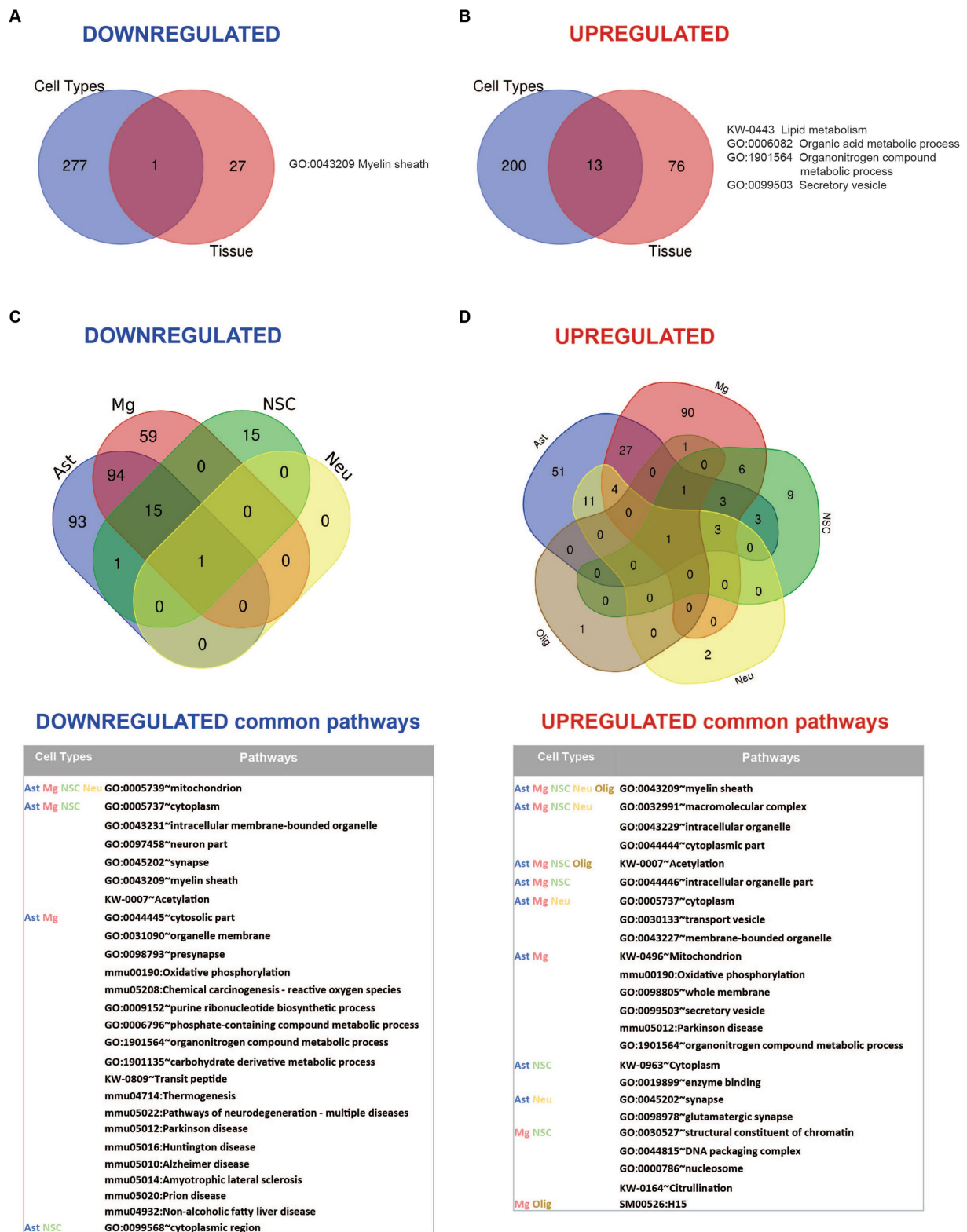


**FIGURE 6** Summary of pathway enrichment analysis showing common and unique findings in whole tissue and isolated brain cells from *Mcoln1<sup>-/-</sup>* mice. **(A)** Venn diagram of common downregulated pathways found in all separate brain cells vs. cortical brain tissue homogenates in *Mcoln1<sup>-/-</sup>* mice. **(B)** Venn diagram of common upregulated pathways found in all separate brain cells vs. cortical brain tissue homogenates in *Mcoln1<sup>-/-</sup>* mice. **(C)** Venn diagram and list of representative common downregulated pathways found in all separate brain cells isolated from *Mcoln1<sup>-/-</sup>* cerebral cortex. **(D)** Venn diagram and list of representative common upregulated pathways found in all separate brain cells isolated from *Mcoln1<sup>-/-</sup>* cerebral cortex.

TABLE 2 Summary of representative up- and downregulated pathways uniquely identified in isolated brain cells from *Mcoln1*<sup>-/-</sup> cerebral cortex.

Cell type	Representative downregulated pathways	FDR	Representative upregulated pathways	FDR
Neurons	none		GO:0098850 Extrinsic component of synaptic vesicle membrane	0.0059
Oligodendrocytes	none		mmu01230 Biosynthesis of amino acids	0.0300
Neural Stem Cells	GO:0042470 Melanosome	8.81E-04	KW-1017 Isopeptide bond	0.0022
	GO:0043531 ADP binding	0.0075	KW-0832 Ubl conjugation	0.0089
	GO:0030864 Cortical actin cytoskeleton	0.0489	GO:0099513 Polymeric cytoskeletal fiber	0.0412
	GO:0031906 Late endosome lumen	0.0888	GO:0005840 Ribosome	0.0423
	GO:004723 Retrograde endocannabinoid signaling	4.15E-04	GO:0098793 Presynapse	1.27E-05
Astrocytes	GO:0045454 Cell redox homeostasis	8.63E-04	GO:0036477 Somatodendritic compartment	0.0017
	GO:0019725 Cellular homeostasis	0.0106	GO:0005885 Arp2/3 protein complex	0.0032
	GO:0005938 Cell cortex	0.012	GO:0005856 Cytoskeleton	0.0092
	GO:0035774 Positive regulation of insulin secretion involved in cellular response to glucose stimulus	0.0296	GO:0014069 Postsynaptic density	0.0270
	GO:0008379 Thioredoxin peroxidase activity	0.0359	GO:0030425 Dendrite	0.0358
	GO:0098754 Detoxification	0.0496	GO:0043204 Perikaryon	0.0358
	GO:0097190 Apoptotic signaling pathway	5.57E-05	GO:0006818 Hydrogen transport	2.54E-05
Microglia	GO:0022626 Cytosolic ribosome	8.64E-05	mmu01212 Fatty acid metabolism	1.85E-04
	DOMAIN EF-hand 1	0.01562	KW-0256 Endoplasmic reticulum	3.34E-04
	KW-1017 Isopeptide bond	0.02414	GO:0019829 Cation-transporting ATPase activity	0.0016
	KW-0488 Methylation	0.02877	mmu00062 Fatty acid elongation	0.0028
			GO:0022853 Active ion transmembrane transporter activity	0.0053
	GO:0002793 Positive regulation of peptide secretion	0.0315	KW-0443 Lipid metabolism	0.0074
	KW-0832 Ubl conjugation	0.04153	KW-0379 Hydroxylation	0.0118
	KW-0944 Nitration	0.09694	GO:0046395 Carboxylic acid catabolic process	0.0130
			GO:0006635 Fatty acid beta-oxidation	0.0253

Importantly, expression of the human myelination genes *MOG*, *MAG*, *MOBP*, *LGI4* and *CNTNAP1* has also been reported in the human MLIV brain sample. Our whole tissue proteomics analysis in the cortex of *Mcoln1*<sup>-/-</sup> mice clearly demonstrated a similar pattern with the broad range of oligodendrocyte and myelin-enriched proteins showing up as significantly downregulated compared to age- and sex-matched control mice (Figure 2). Gene enrichment analysis showed a cluster of myelination, oligodendrocyte differentiation, and axon ensheathment pathways significantly enriched and downregulated (Figure 5; Supplementary Table 5) with GO:0043209 Myelin sheath being the only common downregulated pathway among brain tissue and isolated brain cells proteomes. This data supports our previous findings of reduced myelination in the MLIV mouse brain discussed above.

## 4.2. Lysosome and metabolic changes in the *Mcoln1*<sup>-/-</sup> brain proteome

Another drastic feature of brain pathology in *Mcoln1*<sup>-/-</sup> mice and human MLIV brain is the enlargement of the lysosomal compartment and the accumulation of the lysosomal “storage bodies.” These lysosomal inclusions are structurally and biochemically heterogeneous and contain membranous and granular electron-dense storage due to

the accumulation of undegraded lipids, polysaccharides, and proteins (Tellez-Nagel et al., 1976; Folkerth et al., 1995). Our data confirm these observations on the proteomics level. We report broad upregulation of lysosomal enzymes and structural lysosomal proteins in whole tissue homogenates from *Mcoln1*<sup>-/-</sup> mice, with two of the detected lysosomal enzymes commonly upregulated in whole brain and isolated brain cell data sets (Figures 2, 4B). Using various techniques, including transcriptomics, immunohistochemistry, and enzymatic activity assays, upregulation of lysosomal proteins was commonly reported in other lysosomal storage disorders, such as NPC, Gaucher, mucopolysaccharidoses, and others, and is thought to represent a mechanism to compensate for impaired lysosomal function (Platt et al., 2012; Parenti et al., 2021; Li and Cologna, 2022). A similar increase of lysosomal proteins was reported in the single MLIV brain autopsy proteome, highlighting the universal nature of these observations in the brain tissue across species (Vardi et al., 2021).

We observed upregulation of glycoproteins in *Mcoln1*<sup>-/-</sup> cortex (Table 1). A closer look revealed that many of them are lysosomal hydrolases. Interestingly, we also found a group of glycosylated collagens Col1a1, Col1a2 and Col4a2 significantly elevated in *Mcoln1*<sup>-/-</sup> whole cortex samples. Collagens are a key component of the extracellular matrix (ECM) in the brain and are primarily produced by astrocytes (Platt et al., 2012; Parenti et al., 2021). Some evidence suggests that collagens IV and I may also be produced and play a role

in oligodendrocyte development and function, i.e., adhesion, migration and differentiation of oligodendrocytes during development (Sharma et al., 2015). We did not detect presence of collagens in either isolated astrocytes or oligodendrocytes. Elevated levels of collagens have been reported in neurodegenerative diseases, including Parkinson's (Downs et al., 2022) and multiple sclerosis (Ghorbani and Yong, 2021; Li et al., 2021). Increased vascular collagen IV has been linked to Alzheimer Disease (Lepelletier et al., 2017) and amyotrophic lateral sclerosis (ALS; Garbuzova-Davis and Sanberg, 2014). Accumulations of collagens have also been reported in response to inhibition of autophagy, or more specifically, endoplasmic reticulum (ER)-phagy, a process in which excess collagen is removed via selective targeting for degradation on lysosomes (Forrester et al., 2019; Reggio et al., 2021; Rudinskiy and Molinari, 2023) and is regarded as marker of ER-phagy. Hence, an observed increase in collagens may point to inhibition of this form of autophagy in MLIV, a likely additional consequence of lysosomal function disruption due to loss of TRPML1. Overall, the mechanism leading to increase of collagens in MLIV is unknown and demands further scientific elucidation.

In line with previous reports of lysosomal pathology and lysosomal storage composition, together with the higher abundancies of lysosomal proteins, our pathway analysis on whole brain tissue also showed upregulation of the metabolic and catabolic pathways of lipids and polysaccharides. Importantly, lipid metabolism was one of 7 pathways universally upregulated between brain tissue and all isolated cell types. Proteome analysis of isolated cell types provided deeper insights into lipid metabolism dysregulation, including upregulation of fatty acid metabolism-related pathways unique to microglia.

### 4.3. Mitochondria-related changes identified in *Mcoln1*<sup>-/-</sup> brain cell proteomes

Another group of cellular pathways we found consistently dysregulated in all isolated brain cells, except oligodendrocytes, is related to mitochondrion function and oxidative phosphorylation (Figure 5). Mitochondrion-related dysregulated pathways were very broadly presented in our analysis, particularly in microglia and astrocytes, and, together with the above-mentioned general mitochondrion and oxidative phosphorylation terms, included some more specific structural terms such as mitochondrial envelope, inner membrane, outer membrane, or more narrow parts of the redox chain, such as ATPase or NADH dehydrogenase complex (Supplementary Table 5). Interestingly, while mitochondrial aberrations in the form of fragmentation and decreased mitochondrial Ca<sup>2+</sup> buffering capacity were reported in MLIV patient fibroblasts (Jennings et al., 2006), analysis of mitochondria on electron micrographs in the hippocampus did not report similar structural changes in the *Mcoln1*<sup>-/-</sup> mouse brain (Grishchuk et al., 2014). To our knowledge, this is the first report of mitochondrial changes suggestive of aberrant mitochondrial function in the MLIV mouse. In the literature, presence of fragmented mitochondria in MLIV fibroblasts was hypothesized to be caused by insufficient mitophagy, a process of selective degradation of senescent mitochondria on lysosome as a result of impaired lysosomal function due to loss of TRPML1 function (Jennings et al., 2006). Later, a mechanism of lysosomal-mitochondrial communication was established, where TRPML1 was shown to facilitate direct transfer of Ca<sup>2+</sup> from lysosomes to mitochondria (Peng et al.,

2020). Loss of TRPML1 function in MLIV fibroblasts lead to lower mitochondrial Ca<sup>2+</sup>, reduced lysosome-to-mitochondria contact-dependent transfer of Ca<sup>2+</sup>, and altered lysosome-mitochondrial contact tethering dynamics, with more lysosomes involved and longer tethering contacts in MLIV cells. Authors suggested that lysosome-to-mitochondria TRPML1-mediated Ca<sup>2+</sup> influx can be important to facilitate downstream calcium-dependent mitochondrial functions, including oxidative phosphorylation, motility, and reactive oxygen species (ROS) signaling. Therefore, there is a possibility that either impaired turnover of mitochondria or defective lysosome-mitochondria Ca<sup>2+</sup> transfer caused by loss of TRPML1 function in MLIV may contribute to the broad mitochondrial dysregulation we observed in whole brain tissue and cell-type specific data sets in this study.

Despite the broad overlap in mitochondrial changes between cell types, mitochondria-related pathways were not enriched in whole brain tissue samples. This may be due to low mitochondrial protein sensitivity in whole tissue samples and saturation of the MS detector by proteins that are abundant in brain tissue. This example illustrates the advantage of cell type specific versus whole brain proteomics approach to resolve pathophysiological changes.

### 4.4. Proteome changes in *Mcoln1*<sup>-/-</sup> microglia and astrocytes

Proinflammatory activation of microglia and astrocytes, often referred to as microgliosis and astrocytosis, is a persistent feature of brain pathology in MLIV that is evident in MLIV mouse and human brain tissue starting from the early postnatal (mouse MLIV) and late prenatal (human MLIV) stages of development to the end-stage of disease (Folkerth et al., 1995; Grishchuk et al., 2014; Weinstock et al., 2018; Coughnoux et al., 2019; Zereem et al., 2021). Increased levels of proinflammatory cytokines and chemokines previously reported in MLIV cortical homogenates and astrocyte cultures provide evidence of neuroinflammatory axis in MLIV (Weinstock et al., 2018). Despite this, we previously found that AAV9-mediated gene transfer of *MCOLN1*/TRPML1 directed to neurons was sufficient to fully restore neurologic function in *Mcoln1*<sup>-/-</sup> mice without reducing microgliosis and astrocytosis, therefore dismissing the primary role of these cells in driving MLIV pathogenesis (De Rosa et al., 2021). Studies of *Mcoln1*<sup>-/-</sup> microglia showed decreased expression of microglial surface markers CX3CR1 and CD11b and elevation of markers associated with activation of microglia such as CD86 and MHCII, increased free radical content, expression of iNOS, and shift to glycolytic metabolism (Coughnoux et al., 2019). Transcriptional profiling of freshly isolated CX3CR1<sup>+</sup>CD11b<sup>+</sup>CD45<sup>+</sup> microglia isolated from MLIV mice with subsequent pathway analysis demonstrated changes in lysosomal function, immune cell activation, and neurodegeneration-related gene sets (Coughnoux et al., 2019). Notably, we also see enrichment of neurodegenerative disease-related pathways in microglia in our study. CD86, HIF1a and HIF1a target genes were not resolved in our microglia samples sets. We also did not find immune signaling signature proteins in microglial data sets in our study, including CCL5, which was reported as one of the most significantly overexpressed gene by Coughnoux et al. (2019). These differences can be explained by multiple factors including fewer than optimal to see low abundance proteins starting peptide load due to low cell numbers in original samples, the use of different protocol and antigen markers for microglia isolation resulting in different

population of microglia subsets undergoing analysis, lower protein coverage in our study than transcript coverage in the study by [Cougoux et al. \(2019\)](#), as well as limited translatability between transcriptomic and proteomic abundancies. Remarkably, some of the pathways, i.e., related to apoptosis signaling and cell death, dysregulation of protein synthesis, multiple post-translation modifications alternations, and upregulation of fatty-acid metabolism related pathways, were found only in *Mcoln1*<sup>-/-</sup> microglia.

## 5. Conclusions and future directions

This study provides a protein fingerprint of MLIV brain disease in *Mcoln1*<sup>-/-</sup> mice, confirming previously known pathological hallmarks and adding new depth to the understanding of the molecular changes and pathways underlying the disease. Both LC-MS/MS proteomics approaches, using either whole tissue or isolated cell type-specific fractions, were synergistic in providing detailed information on the proteome signature of MLIV. The major observations at the level of whole brain tissue were downregulation of myelination-related pathways, and upregulation of calcium, lysosome, and metabolic pathways, including lipids and carbohydrates. While analyzing proteomes of *Mcoln1*<sup>-/-</sup> neurons, neural stem cells, astrocytes, microglia, and oligodendrocytes, we found commonly dysregulated pathways between these cell types that included organellar membrane, membrane protein complexes, mitochondria and oxidative phosphorylation, synapse composition, lipid metabolism, chromatin organization, secretory or transport vesicles, and some post-translational protein modifications. This portfolio of pathways creates a signature of the common alterations in cells in response to loss of TRPML1 function. Additionally, our analysis also showed cell-type specific responses to loss of TRPML1 that might be especially insightful for understanding the role of this lysosomal channel in a cell type specific setting. We found that among all studied cell types, despite strong hypomyelination phenotype in MLIV, isolated O4+ *Mcoln1*<sup>-/-</sup> oligodendrocytes had minimal changes at the level of proteome when compared to oligodendrocytes from the age- and sex-matched controls. Major changes in neurons were found in proteins related to mitochondria, myelin sheath, and synaptic membrane organization. In addition to this, in neural stem cells, pathways related to melanosomes and protein synthesis were enriched. Yet, the highest number of dysregulated pathways were found in microglia and astrocytes, that, together with neurodegeneration-related, membrane organization, metabolic and mitochondria-related pathways commonly enriched in both populations, also showed a signature of distinct, specific changes. In astrocytes, these changes included cytoskeleton-, cell homeostasis-, endocannabinoid signaling-, and postsynaptic membrane-related pathways, whereas microglia showed enriched protein synthesis, endoplasmic-reticulum-related, fatty acid metabolism, and regulation apoptosis pathways.

Our data provide a helpful insight into potential molecular biomarkers of MLIV. Since TRPML1 is a transmembrane lysosomal channel, any *in-vitro* assay reporting restoration of its function for future efficacy and potency assay development has to rely on direct measurement of its ion conduction which presents technical challenges. Even more importantly, easily accessible surrogate biomarkers that could report activity of TRPML1 in accessible

tissues, such as serum or plasma, for translational and interventional studies are currently missing. Our study provides insight into potential molecular biomarkers for future validation. For example, based on our data, hexosaminidase B (HEXB) and tripeptidyl-peptidase 1 (TPP1) could be possible biomarker candidates. Both proteins are lysosomal enzymes, and loss of their function is responsible for neurodegenerative lysosomal diseases Tay-Sachs (HEXB) or Neuronal Ceroid Lipofuscinosis 2 (CLN2). We report increased abundances of TPP1 and HEXB in response to TRPML1 loss in both brain tissue and brain cells data sets. This suggests either their compensatory upregulation in response to lysosomal dysfunction or reflects enlargement of the lysosomal compartment due to impaired lysosomal turnover. In addition to increased abundancies observed by LC-MS/MS, we showed increase of active TPP1 in *Mcoln1*<sup>-/-</sup> brain tissue by Western blot. Gene transfer of the functional human *MCOLN1* transgene using an AAV-mediated approach shown to prevent motor disfunction and restore brain pathology in *Mcoln1*<sup>-/-</sup> mice, resulted in correction of TPP1 levels, further supporting its potential as a biomarker candidate. Future studies will be required to validate the use of TPP1, HEXB, or other lysosomal proteins as biomarkers for MLIV.

## Data availability statement

The datasets presented in this study can be found in online repositories. The names of the repository/repositories and accession number(s) can be found in the article/[Supplementary material](#).

## Ethics statement

The animal study was reviewed and approved by Mass General EXECUTIVE COMMITTEE ON RESEARCH.

## Author contributions

BB and YG contributed to conception and design of the study, data interpretation, and wrote manuscript. MS, MC, ML, and ZN performed experiments. SS performed data analysis for this study. MS and SS contributed to manuscript writing. BB created a data repository. All authors contributed to the article and approved the submitted version.

## Funding

Authors received funding for research from Mucopolipidosis Type IV Foundation.

## Conflict of interest

YG is an inventor on US patent application PCT/US2020/057839 titled GENE THERAPY APPROACHES TO MUCOLIPIDOSIS IV (MLIV) assigned to Massachusetts General Brigham Corporation.

The remaining authors declare that the research was conducted in the absence of any commercial or financial relationships that could be construed as a potential conflict of interest.

## Publisher's note

All claims expressed in this article are solely those of the authors and do not necessarily represent those of their affiliated organizations, or those of the publisher, the editors and the

reviewers. Any product that may be evaluated in this article, or claim that may be made by its manufacturer, is not guaranteed or endorsed by the publisher.

## Supplementary material

The Supplementary material for this article can be found online at: <https://www.frontiersin.org/articles/10.3389/fnmol.2023.1215425/full#supplementary-material>

## References

- Altarescu, G., Sun, M., Moore, D. F., Smith, J. A., Wiggs, E. A., Solomon, B. I., et al. (2002). The neurogenetics of mucopolipidosis type IV. *Neurology* 59, 306–313. doi: 10.1212/WNL.59.3.306
- Bonavita, S., Virta, A., Jeffries, N., Goldin, E., Tedeschi, G., and Schiffmann, R. (2003). Diffuse neuroaxonal involvement in mucopolipidosis IV as assessed by proton magnetic resonance spectroscopic imaging. *J. Child Neurol.* 18, 443–449. doi: 10.1177/08830738030180070701
- Boudewyn, L. C., Sikora, J., Kuchar, L., Ledvinova, J., Grishchuk, Y., Wang, S. L., et al. (2017). N-butyldeoxyjirimycin delays motor deficits, cerebellar microgliosis, and Purkinje cell loss in a mouse model of mucopolipidosis type IV. *Neurobiol. Dis.* 105, 257–270. doi: 10.1016/j.nbd.2017.06.003
- Chitayat, D., Meunier, C. M., Hodgkinson, K. A., Silver, K., Flanders, M., Anderson, I. J., et al. (1991). Mucopolipidosis type IV: clinical manifestations and natural history. *Am. J. Med. Genet.* 41, 313–318. doi: 10.1002/ajmg.1320410310
- Cookson, M. R. (2019). Proteomics: techniques and applications in neuroscience. *J. Neurochem.* 151, 394–396. doi: 10.1111/jnc.14867
- Cougnoux, A., Drummond, R. A., Fellmeth, M., Navid, F., Collar, A. L., Iben, J., et al. (2019). Unique molecular signature in mucopolipidosis type IV microglia. *J. Neuroinflammation* 16:276. doi: 10.1186/s12974-019-1672-4
- Davis, R. G., Park, H. M., Kim, K., Greer, J. B., Fellers, R. T., LeDuc, R. D., et al. (2018). Top-down proteomics enables comparative analysis of brain Proteoforms between mouse strains. *Anal. Chem.* 90, 3802–3810. doi: 10.1021/acs.analchem.7b04108
- De Rosa, S., Salani, M., Smith, S., Sangster, M., Miller-Browne, V., Wassmer, S., et al. (2021). MCOLN1 gene therapy corrects neurologic dysfunction in the mouse model of mucopolipidosis IV. *Hum. Mol. Genet.* 30, 908–922. doi: 10.1093/hmg/ddab093
- Downs, M., Sethi, M. K., Raghunathan, R., Layne, M. D., and Zaia, J. (2022). Matrisome changes in Parkinson's disease. *Anal. Bioanal. Chem.* 414, 3005–3015. doi: 10.1007/s00216-022-03929-4
- Drulis-Fajdasz, D., Gostomska-Pampuch, K., Duda, P., Wisniewski, J. R., and Rakus, D. (2021). Quantitative proteomics reveals significant differences between mouse brain formations in expression of proteins involved in neuronal plasticity during aging. *Cells* 10. doi: 10.3390/cells10082021
- Folkerth, R. D., Alroy, J., Lomakina, I., Skutelsky, E., Raghavan, S. S., and Kolodny, E. H. (1995). Mucopolipidosis IV: morphology and histochemistry of an autopsy case. *J. Neuropathol. Exp. Neurol.* 54, 154–164. doi: 10.1097/00005072-199503000-00002
- Forrester, A., De Leonibus, C., Grumati, P., Fasana, E., Piemontese, M., Staiano, L., et al. (2019). A selective ER-phagy exerts procollagen quality control via a Calnexin-FAM134B complex. *EMBO J.* 38:e99847. doi: 10.15252/embj.201899847
- Frei, K. P., Patronas, N. J., Crutchfield, K. E., Altarescu, G., and Schiffmann, R. (1998). Mucopolipidosis type IV: characteristic MRI findings. *Neurology* 51, 565–569. doi: 10.1212/WNL.51.2.565
- Garbuzova-Davis, S., and Sanberg, P. R. (2014). Blood-CNS barrier impairment in ALS patients versus an animal model. *Front. Cell. Neurosci.* 8:21. doi: 10.3389/fncel.2014.00021
- Ghorbani, S., and Yong, V. W. (2021). The extracellular matrix as modifier of neuroinflammation and remyelination in multiple sclerosis. *Brain* 144, 1958–1973. doi: 10.1093/brain/awab059
- Grishchuk, Y., Pena, K. A., Coblentz, J., King, V. E., Humphrey, D. M., Wang, S. L., et al. (2015). Impaired myelination and reduced brain ferric iron in the mouse model of mucopolipidosis IV. *Dis. Model. Mech.* 8, 1591–1601. doi: 10.1242/dmm.021154
- Grishchuk, Y., Sri, S., Rudinskiy, N., Ma, W., Stember, K. G., Cottle, M. W., et al. (2014). Behavioral deficits, early gliosis, dysmyelination and synaptic dysfunction in a mouse model of mucopolipidosis IV. *Acta Neuropathol. Commun.* 2:133. doi: 10.1186/s40478-014-0133-7
- Grishchuk, Y., Stember, K. G., Matsunaga, A., Olivares, A. M., Cruz, N. M., King, V. E., et al. (2016). Retinal dystrophy and optic nerve pathology in the mouse model of Mucopolipidosis IV. *Am. J. Pathol.* 186, 199–209. doi: 10.1016/j.ajpath.2015.09.017
- Jennings, J. J. Jr., Zhu, J. H., Rbaibi, Y., Luo, X., Chu, C. T., and Kiselyov, K. (2006). Mitochondrial aberrations in mucopolipidosis type IV. *J. Biol. Chem.* 281, 39041–39050. doi: 10.1074/jbc.M607982200
- Lepelletier, F. X., Mann, D. M., Robinson, A. C., Pinteaux, E., and Boutin, H. (2017). Early changes in extracellular matrix in Alzheimer's disease. *Neuropathol. Appl. Neurobiol.* 43, 167–182. doi: 10.1111/nan.12295
- Li, M., Chen, H., Yin, P., Song, J., Jiang, F., Tang, Z., et al. (2021). Identification and clinical validation of key extracellular proteins as the potential biomarkers in relapsing-remitting multiple sclerosis. *Front. Immunol.* 12:753929. doi: 10.3389/fimmu.2021.753929
- Li, W., and Cologna, S. M. (2022). Mass spectrometry-based proteomics in neurodegenerative lysosomal storage disorders. *Mol. Omics.* 18, 256–278. doi: 10.1039/D2MO00004K
- Lin, L., Sohar, I., Lackland, H., and Lobel, P. (2001). The human CLN2 protein/tripeptidyl-peptidase I is a serine protease that autoactivates at acidic pH. *J. Biol. Chem.* 276, 2249–2255. doi: 10.1074/jbc.M008562200
- Mann, M., Kulak, N. A., Nagaraj, N., and Cox, J. (2013). The coming age of complete, accurate, and ubiquitous proteomes. *Mol. Cell* 49, 583–590. doi: 10.1016/j.molcel.2013.01.029
- Mela, A., and Goldman, J. E. (2009). The tetraspanin KAI1/CD82 is expressed by late-lineage oligodendrocyte precursors and may function to restrict precursor migration and promote oligodendrocyte differentiation and myelination. *J. Neurosci.* 29, 11172–11181. doi: 10.1523/JNEUROSCI.3075-09.2009
- Mela, A., and Goldman, J. E. (2013). CD82 blocks cMet activation and overcomes hepatocyte growth factor effects on oligodendrocyte precursor differentiation. *J. Neurosci.* 33, 7952–7960. doi: 10.1523/JNEUROSCI.5836-12.2013
- Mepyans, M., Andrzejczak, L., Sosa, J., Smith, S., Herron, S., DeRosa, S., et al. (2020). Early evidence of delayed oligodendrocyte maturation in the mouse model of mucopolipidosis type IV. *Dis. Model. Mech.* 13. doi: 10.1242/dmm.044230
- Micsenyi, M. C., Dobrenis, K., Stephney, G., Pickel, J., Vanier, M. T., Slaugenhaupt, S. A., et al. (2009). Neuropathology of the Mcoln 1(–/–) knockout mouse model of mucopolipidosis type IV. *J. Neuropathol. Exp. Neurol.* 68, 125–135. doi: 10.1097/NEN.0b013e3181942cf0
- Misko, A., Grishchuk, Y., Goldin, E., and Schiffmann, R. (1993) in *Mucopolipidosis IV*. eds. M. P. Adam, H. H. Ardinger, R. A. Pagon, S. E. Wallace, B. L. J. and G. Mirzaet al. (Seattle (WA): Gene reviews((R)))
- Misko, A., Wood, L., Kiselyov, K., Slaugenhaupt, S., and Grishchuk, Y. (2021). Progress in elucidating pathophysiology of mucopolipidosis IV. *Neurosci. Lett.* 755:135944. doi: 10.1016/j.neulet.2021.135944
- Parenti, G., Medina, D. L., and Ballabio, A. (2021). The rapidly evolving view of lysosomal storage diseases. *EMBO Mol. Med.* 13:e12836. doi: 10.15252/emmm.202012836
- Peng, W., Wong, Y. C., and Krainc, D. (2020). Mitochondria-lysosome contacts regulate mitochondrial Ca<sup>2+</sup> dynamics via lysosomal TRPML1. *Proc. Natl. Acad. Sci. U. S. A.* 117, 19266–19275. doi: 10.1073/pnas.2003236117
- Platt, F. M., Boland, B., and van der Spoel, A. C. (2012). The cell biology of disease: lysosomal storage disorders: the cellular impact of lysosomal dysfunction. *J. Cell Biol.* 199, 723–734. doi: 10.1083/jcb.201208152
- Rayaprolu, S., Bitarafan, S., Santiago, J. V., Betarbet, R., Sunna, S., Cheng, L., et al. (2022). Cell type-specific biotin labeling in vivo resolves regional neuronal and astrocyte proteomic differences in mouse brain. *Nat. Commun.* 13:2927. doi: 10.1038/s41467-022-30623-x
- Reggio, A., Buonomo, V., Berkane, R., Bhaskara, R. M., Tellechea, M., Peluso, I., et al. (2021). Role of FAM134 paralogues in endoplasmic reticulum remodeling, ER-phagy, and collagen quality control. *EMBO Rep.* 22:e52289. doi: 10.15252/embr.202052289
- Rudinskiy, M., and Molinari, M. (2023). ER-to-lysosome-associated degradation in a nutshell: mammalian, yeast, and plant ER-phagy as induced by misfolded proteins. *FEBS Lett.* doi: 10.1002/1873-3468.14674 [Epub ahead of print].



- Schiffmann, R., Mayfield, J., Swift, C., and Nestrasil, I. (2014). Quantitative neuroimaging in mucopolipidosis type IV. *Mol. Genet. Metab.* 111, 147–151. doi: 10.1016/j.ymgme.2013.11.007
- Sharma, K., Schmitt, S., Bergner, C. G., Tyanova, S., Kannaiyan, N., Manrique-Hoyos, N., et al. (2015). Cell type- and brain region-resolved mouse brain proteome. *Nat. Neurosci.* 18, 1819–1831. doi: 10.1038/nn.4160
- Sherman, B. T., Hao, M., Qiu, J., Jiao, X., Baseler, M. W., Lane, H. C., et al. (2022). DAVID: a web server for functional enrichment analysis and functional annotation of gene lists (2021 update). *Nucleic Acids Res.* 50, W216–W221. doi: 10.1093/nar/gkac194
- Specht, H., Harmange, G., Perlman, D. H., Emmott, E., Niziolek, Z., Budnik, B., et al. (2018). Automated sample preparation for high-throughput single-cell proteomics. *bioRxiv:399774*
- Tellez-Nagel, I., Rapin, I., Iwamoto, T., Johnson, A. B., Norton, W. T., and Nitowsky, H. (1976). Mucopolipidosis IV. Clinical, ultrastructural, histochemical, and chemical studies of a case, including a brain biopsy. *Arch. Neurol.* 33, 828–835. doi: 10.1001/archneur.1976.00500120032005
- Vardi, A., Pri-Or, A., Wigoda, N., Grishchuk, Y., and Futerman, A. H. (2021). Proteomics analysis of a human brain sample from a mucopolipidosis type IV patient reveals pathophysiological pathways. *Orphanet J. Rare Dis.* 16:39. doi: 10.1186/s13023-021-01679-7
- Venugopal, B., Browning, M. F., Curcio-Morelli, C., Varro, A., Michaud, N., Nanthakumar, N., et al. (2007). Neurologic, gastric, and ophthalmologic pathologies in a murine model of mucopolipidosis type IV. *Am. J. Hum. Genet.* 81, 1070–1083. doi: 10.1086/521954
- Weinstock, L. D., Furness, A. M., Herron, S. S., Smith, S. S., Sankar, S. B., DeRosa, S. G., et al. (2018). Fingolimod phosphate inhibits astrocyte inflammatory activity in mucopolipidosis IV. *Hum. Mol. Genet.* 27, 2725–2738. doi: 10.1093/hmg/ddy182
- Wilhelm, M., Schlegl, J., Hahne, H., Gholami, A. M., Lieberenz, M., Savitski, M. M., et al. (2014). Mass-spectrometry-based draft of the human proteome. *Nature* 509, 582–587. doi: 10.1038/nature13319
- Wolf, N. I., Ffrench-Constant, C., and van der Knaap, M. S. (2021). Hypomyelinating leukodystrophies - unravelling myelin biology. *Nat. Rev. Neurol.* 17, 88–103. doi: 10.1038/s41582-020-00432-1
- Ximerakis, M., Lipnick, S. L., Innes, B. T., Simmons, S. K., Adiconis, X., Dionne, D., et al. (2019). Single-cell transcriptomic profiling of the aging mouse brain. *Nat. Neurosci.* 22, 1696–1708. doi: 10.1038/s41593-019-0491-3
- Zerem, A., Ben-Sira, L., Vigdorovich, N., Leibovitz, Z., Fisher, Y., Schiffmann, R., et al. (2021). White matter abnormalities and iron deposition in prenatal mucopolipidosis IV-fetal imaging and pathology. *Metab. Brain Dis.* 36, 2155–2167. doi: 10.1007/s11011-021-00742-3